Magnetic superlattices and their nanoscale phase transition effects

Jinwoo Cheon*†, Jong-Il Park‡, Jin-sil Choi*, Young-wook Jun*, Sehun Kim‡, Min Gyu Kim§, Young-Min Kim¶, and Youn Joong Kim¶

*Department of Chemistry and Nano-Medical National Core Research Center, Yonsei University, Seoul 120-749, Korea; ‡Department of Chemistry, Korea Advanced Institute of Science and Technology, Daejeon 305-701, Korea; §Pohang Accelerator Laboratory, Pohang 790-784, Korea; and ¶Division of Nano-Material and Environmental Science, Korea Basic Science Institute, Daejeon 305-333, Korea

Edited by Louis E. Brus, Columbia University, New York, NY, and approved December 29, 2005 (received for review October 11, 2005)

The systematic assembly of nanoscale constituents into highly ordered superlattices is of significant interest because of the potential of their multifunctionalities and the discovery of new collective properties. However, successful observations of such superlattice-associated nanoscale phenomena are still elusive. Here, we present magnetic superlattices of Co and Fe_3O_4 nanoparticles with multidimensional symmetry of either AB (NaCl) or AB_2 (AlB_2). The discovery of significant enhancement (≈25 times) of ferrimagnetism is further revealed by forming previously undescribed superlattices of magnetically soft–hard Fe_3O_4@$CoFe_2O_4$ through the confined geometrical effect of thermally driven intrasuperlattice phase transition between the nanoparticulate components.

binary superlattices | magnetic nanoparticle

Early investigations of nanoparticle assembly have focused on the fabrication of ordered monomeric nanoparticle superlattices with specific packing symmetry (e.g., fcc, hcp) (1–4), and the novel properties arising from these assemblies have been elucidated, such as metal–insulator transitions (2) and band-gap engineering (3). Researchers have further explored ordered binary superlattice systems composed of nanoparticle components that are isostructural with binary crystals of atoms such as NaCl (5), AlB_2 (6–8), and $NaZn_{13}$ (8). Ordered two-dimensional (2D) arrays of gold nanoparticles with bimodal size distribution have been reported (6), and further studies have included binary assemblies of gold and silver nanoparticles (6) and of FePt and Fe_3O_4 in which the interesting magnetic phenomenon of exchange-coupled magnetism (9) has been observed. These methods have been extended to three dimensions as demonstrated in the binary assembly of PbSe and γ-Fe_2O_3 nanoparticles (8, 10). Although multimodal superlattices have the potential for the development of advanced nanoarchitectural systems with enhanced properties or multifunctional capabilities, studies on their fabrication and the nanoscale phenomena arising from the assembly are still in its early stages. Here, we present three-dimensionally (3D) ordered binary magnetic superlattices constructed through the coassembly of Fe_3O_4 and Co nanoparticles. By elucidating the effects of relative particle size ratio and stoichiometry ratio on the formation of superlattices, we have developed methods to control the assembled geometry starting from a separated phase and progressing to simple mixed assemblies and highly ordered AB- and AB_2-type binary superlattices. These binary magnetic nanoparticle superlattice systems exhibit a phase transformation to a previously undescribed superlattice of core–shell type Fe_3O_4@$CoFe_2O_4$ through thermally driven nanoscale diffusion and redox chemical-reaction processes between symmetrically adjacent nanoparticle components.

Results and Discussion

When hard spheres of two different sizes are mixed together, these spheres tend to assemble into a new structure with maximum packing density (11–13). Two crucial parameters determine the binary assembly pattern of the spheres: (*i*) the size ratio ($\gamma = R_{small}/R_{large}$) and (*ii*) the stoichiometric ratio between two spheres. Although the binary organization of colloidal nanoparticle systems can be predicted by such hard sphere assembly approximations (5–10, 14), other parameters such as interparticle potentials also contribute to the determination of assembly patterns (10, 14).

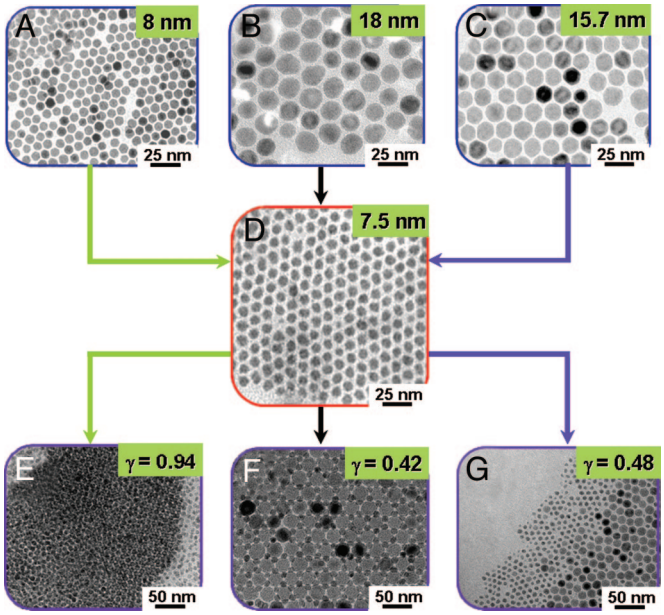

Fig. 1. Binary Fe_3O_4 and Co nanoparticle assemblies and their relative size ratio effect ($\gamma = R_{Co}/R_{Fe_3O_4}$). (*A–C*) Fe_3O_4 nanoparticles of 8.0 (*A*), 18.0 (*B*), and 15.7 (*C*) nm. (*D*) Co nanoparticles of 7.5 nm. (*E–G*) Binary assemblies of Fe_3O_4 and Co nanoparticles. The assembly patterns are systematically modulated as random mixtures ($\gamma = 0.94$) (*E*), well organized binary superlattices ($\gamma = 0.42$) (*F*), and phase-separated arrays ($\gamma = 0.48$) (*G*).

Binary superlattices of magnetic Fe_3O_4 and Co nanoparticles were examined with careful consideration of such size ratio and stoichiometric ratio effects. The Fe_3O_4 nanoparticles used are highly monodispersed ($\sigma \approx 5\%$), and the size can be tuned from 8.0 nm to 15.7 and 18.0 nm (Fig. 1 *A–C*) by controlling the growth parameters during the thermal reaction of $Fe(CO)_5$ in a hot dioctylether solution containing lauric acid (15). Co nanoparticles of 7.5 nm with narrow size distribution ($\sigma \approx 7\%$) were synthesized by thermal decomposition of $Co_2(CO)_8$ in toluene containing NaAOT [AOT, bis(2-ethylhexyl)sulfosuccinate] (Fig.

Conflict of interest statement: No conflicts declared.

This paper was submitted directly (Track II) to the PNAS office.

Abbreviation: TEM, transmission electron microscopic.

†To whom correspondence should be addressed. E-mail: jcheon@yonsei.ac.kr.

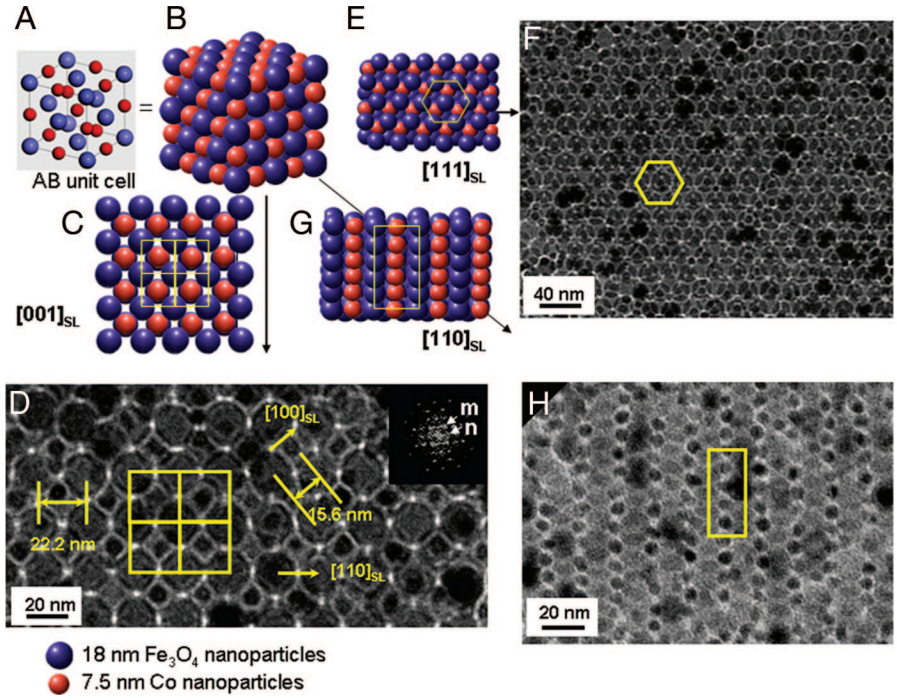

Fig. 2. Binary superlattices of Fe_3O_4 and Co nanoparticles with AB symmetry and their structural characterizations. (*A* and *B*) The unit cell (*A*) and the extended cell (*B*) of the NaCl type AB binary structure. (*C–H*) TEM images of our binary superlattices (*D*, *F*, and *H*) and the corresponding AB structure (*C*, *E*, and *G*), respectively, which match the $[001]_{SL}$, $[111]_{SL}$, and $[110]_{SL}$ projection of the AB structure. TEM analyses suggest our binary superlattices are of AB symmetry. Each Co nanoparticle is surrounded by six equidistant Fe_3O_4 nanoparticles situated at the corner of an octahedron (yellow squares), as is the case for each Fe_3O_4 nanoparticle surrounded by six Co nanoparticles. Our superlattices have periodicities with interplanar distances of 15.6 nm for $(200)_{SL}$ and 22.2 nm for $(110)_{SL}$, which is consistent with the Fourier transform of the TEM image (*D Inset*). The inner spots marked m and n spots are contributed from $[200]_{SL}$ and $[110]_{SL}$ reflections, respectively.

1*D*; ref. 16). First, the size ratio effect on their binary assemblies was examined by varying the size of the Fe_3O_4 nanoparticles while keeping the Co nanoparticle size fixed. Randomly mixed binary structures were observed when one equivalent of 8.0-nm Fe_3O_4 was mixed with a 7.5-nm Co nanoparticle solution [$\gamma(R_{Co}/R_{Fe_3O_4}) = 0.94$] and cocrystallized on a carbon-coated Cu grid by slow evaporation of solvent (Fig. 1*E*), whereas highly ordered 3D superlattices resulted when larger, 18.0-nm Fe_3O_4 nanoparticles were mixed with the Co nanoparticles ($\gamma = 0.42$) (Fig. 1*F*). In contrast, when 15.7-nm Fe_3O_4 nanoparticles were used ($\gamma = 0.48$), separated phases of nanoparticles were dominant (Fig. 1*G*). These results suggest that the size ratio is crucial for the formation of binary assemblies of nanoparticles (5–10, 14). To examine the packing symmetry of the binary superlattices obtained at $\gamma = 0.42$, transmission electron microscopic (TEM) investigations along the various crystallographic directions were performed. Fig. 2 shows the unit cell structure and 2D projections of AB structures, respectively (5). The unit cell is cubic, and the structure consists of two interpenetrating face-centered arrays of Co and Fe_3O_4 nanoparticles (NaCl type; space group 225). Each Co nanoparticle is surrounded by six equidistant Fe_3O_4 nanoparticles situated at the corners of an octahedron. Similarly, each Fe_3O_4 nanoparticle is surrounded by six Co nanoparticles. As shown in Fig. 2*D*, a TEM image of the binary superlattice corresponds with the $[001]_{SL}$ projection of AB structures (Fig. 2*C*). Alternative views of the binary structure shown in Fig. 2 *F* and *H* are consistent with the $[111]_{SL}$ and $[110]_{SL}$ projections of the AB structure (Fig. 2 *E* and *G*), respectively. Our superlattices have periodicities with interplanar distances of 15.6 nm for $(200)_{SL}$ and 22.2 nm for $(110)_{SL}$ (Fig. 2*D*), which are observed as discrete reflection spots in the Fourier-transformed TEM images. From these observations, we conclude the binary superlattices are well organized AB structures with the lattice parameter of 31.2 nm.

We further investigated the effects of the relative stoichiometry of Fe_3O_4 and Co nanoparticles on assembly patterns of binary superlattices. When Fe_3O_4 nanoparticles and two molar excess of Co nanoparticle were mixed and cocrystallized, the resulting superlattices (Fig. 3*E*) revealed that the nanoparticles assembled into an AB_2 rather than an AB structure. The structures show bilayers composed of a hexagonal close-packed layer of Fe_3O_4 and a second layer of Co nanoparticles. The observed bilayer structure (Fig. 3*E*) is the hexagonal AB_2 substructure (Fig. 3 *A–C*) and has periodicities with interplanar distances of 9.6 nm for $(200)_{SL}$ and 16.7 nm for $(110)_{SL}$. A small-angle diffraction pattern of our bilayer structure (Fig. 3*D*) shows discrete reflection spots from the hexagonally ordered structures. The inner hexagonal spots marked p and q positioned 30° apart from each other are contributions from the $(200)_{SL}$ and $(110)_{SL}$ reflections, respectively.

The formation of binary magnetic nanoparticle superlattices with well defined symmetry and stoichiometric composition prompted us to investigate their assembly-induced novel magnetic properties. Because each Fe_3O_4 nanoparticle is surrounded by a highly symmetric arrangement of Co nanoparticles within a distance of $\approx$1 nm, nanoscale chemical and physical interactions between these two nanoparticles can be exploited to generate unique phase-transitional behaviors. The nanoscale transformation of as-assembled binary superlattices of Fe_3O_4 and Co nanoparticles into core–shell type $Fe_3O_4@CoFe_2O_4$ superlattices were thermally driven through intrasuperlattice redox chemical processes. Such core–shell type $Fe_3O_4@CoFe_2O_4$ superlattice formation leads to significant changes in its magnetism when compared with those of as-assembled superlattices. As-assembled AB type superlattices (Fig. 4*A*) have magnetic coercivity (H_c) values of 580 oersted (Oe) at 5 K (Fig. 4*C*), which is roughly in between the values for individual Co (780 Oe) and Fe_3O_4 (200 Oe) nanoparticles. After thermal annealing pro-

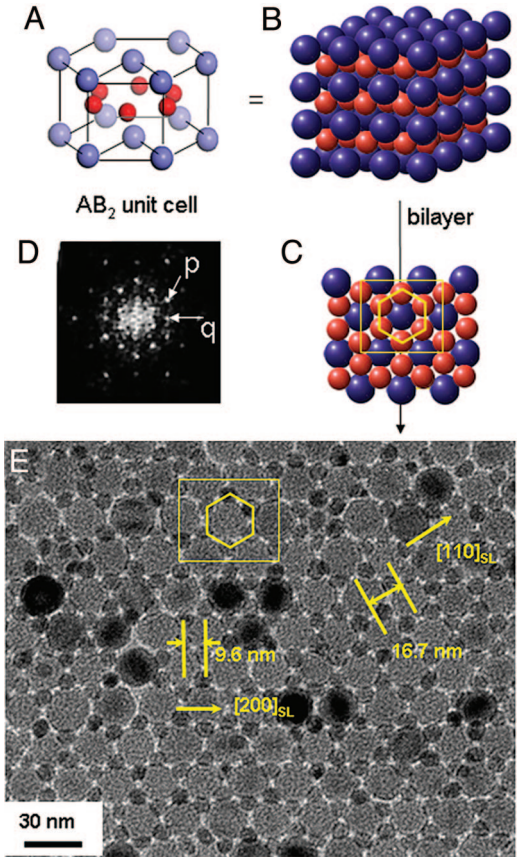

Fig. 3. Binary superlattices of Fe_3O_4 (18.0 nm) and Co nanoparticles (7.5 nm) with AB_2 symmetry. (*A–C*) Figures of the unit cell (*A*), the extended cell (*B*), and bilayers along *c* axis (*C*) of the hexagonal AB_2 binary structure. (*D*) Small-angle electron diffraction (SAED) pattern of AB_2 bilayers. The hexagonal spots marked p and q in ED pattern are contributed from a periodicity of 9.6 and 16.7 nm in TEM image, respectively. (*E*) TEM image of our AB_2 superlattices. Fe_3O_4 nanoparticles form a hexagonally close-packed layer, and Co nanoparticles form a second layer (yellow hexagon), which are situated in the interstices of Fe_3O_4 layers. The measured interplanar distances are 9.6 and 16.7 nm for $(200)_{SL}$ and $(110)_{SL}$, which are consistent with the SAED results.

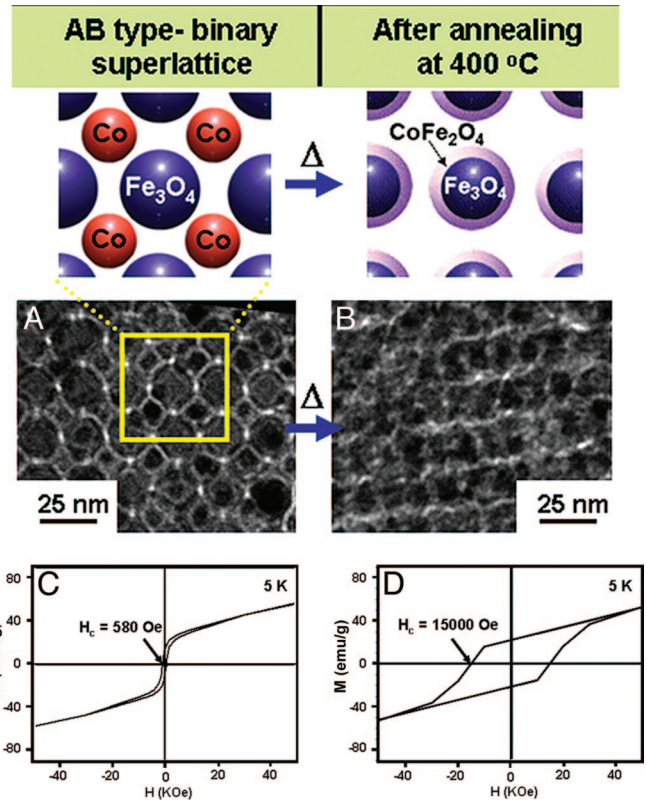

Fig. 4. Thermally induced assembly phase transformation from soft–soft Fe_3O_4 and Co binary superlattices to soft–hard core–shell type Fe_3O_4@$CoFe_2O_4$ nanoparticle superlattices with enhancement in ferrimagnetism. (*A* and *B*) TEM images of as-assembled (*A*) and annealed (*B*) AB type superlattices. After thermal annealing processes at 400°C, the structural integrity of the superlattices is retained, whereas intercalated Co nanoparticles in as-assembled binary superlattices disappear. (*C* and *D*) Hysteresis loops of as-assembled (*C*) and annealed (*D*) AB type superlattices. After thermal treatment, a dramatic enhancement (≈25 times) in magnetic coercivity is observed.

cesses at 400°C (Fig. 4*B*), however, the magnetic coercivity of AB structures increased dramatically to 15,000 Oe (≈25 times higher than the initial value) (Fig. 4*D*; refs. 17 and 18). However, such dramatic magnetic enhancement is not observed for phase-segregated mixtures of Fe_3O_4 and Co nanoparticles (see Fig. 7, which is published as supporting information on the PNAS web site), suggesting that symmetry and proximity effects between the two nanoparticle components are essential in inducing such nanoscale magnetic phenomena.

As depicted in Fig. 5 *A* and *B*, the transformation processes can involve (*i*) dissolution and diffusion of Co atoms from Co nanoparticles into a Fe_3O_4 inverse spinel matrix and (*ii*) alloying of Co and Fe_3O_4 through exchange of Fe^{2+} in an O_h site with a Co atom through redox chemical reactions in which a Co atom is oxidized at the expense of an Fe^{2+}, which ultimately results in the formation of the superlattices of core–shell type Fe_3O_4@$CoFe_2O_4$ nanoparticles.

The formation of core–shell type Fe_3O_4@$CoFe_2O_4$ nanoparticles resulting from such phase transformation processes was confirmed by elemental mapping analyses using high-resolution TEM. Because it is difficult to perform the elemental analyses with multilayers of nanoparticles, annealed nanoparticles were redispersed in toluene by using sonication and resampled on a TEM grid. Elemental mapping analyses based on Fe L-edge (color-coded as yellow; Fig. 6*A*) and Co L-edge (color-coded as cyan; Fig. 6*B*) electron energy loss spectroscopy show that the nanoparticles contain both iron and cobalt. An overlay of these two images (Fig. 6 *C* and *D*) clearly indicates that the core region has high Fe content (yellow color). In contrast, the shell region shows green color resulting from color mixing between yellow (i.e., Fe) and cyan (i.e., Co), which is indicative of coexistence of Fe and Co at the shell region. These results strongly support that nanoparticles possess core–shell structure of Fe_3O_4@$CoFe_2O_4$ (Fig. 6 *D* and *E*).

X-ray absorption spectroscopic analyses provide supporting evidence for such phase-transformation processes of the binary superlattices (Fig. 5 *C–E*). In the Co K-edge x-ray absorption near-edge structure (XANES) spectra of our AB-type Fe_3O_4 and Co superlattices (Fig. 5*C*), the gradual decrease of the shoulder intensities at 7,712 eV (1 eV = 1.602×10^{-19} J) upon annealing at 300° and 400°C, respectively, suggests the disappearance of Co metallic species (19). The main-edge peak feature changes from a broad peak at 7,725 eV into two peaks at 7,723 and 7,728 eV and is indicative of the formation of Co^{II} species (20, 21). These spectral changes indicate that the metallic Co atoms are oxidized to Co^{2+} ions surrounded by T_d or O_h oxygen lattices upon thermal annealing. The Fe K-edge XANES spectra (Fig. 5*D*) of as-assembled structures exhibit a pre-edge peak at 7,715 eV originating from Fe^{3+} in the T_d site of the inverse spinel lattice and a broad main-edge peak at ≈7,130 eV due to Fe^{2+} and Fe^{3+} in the O_h

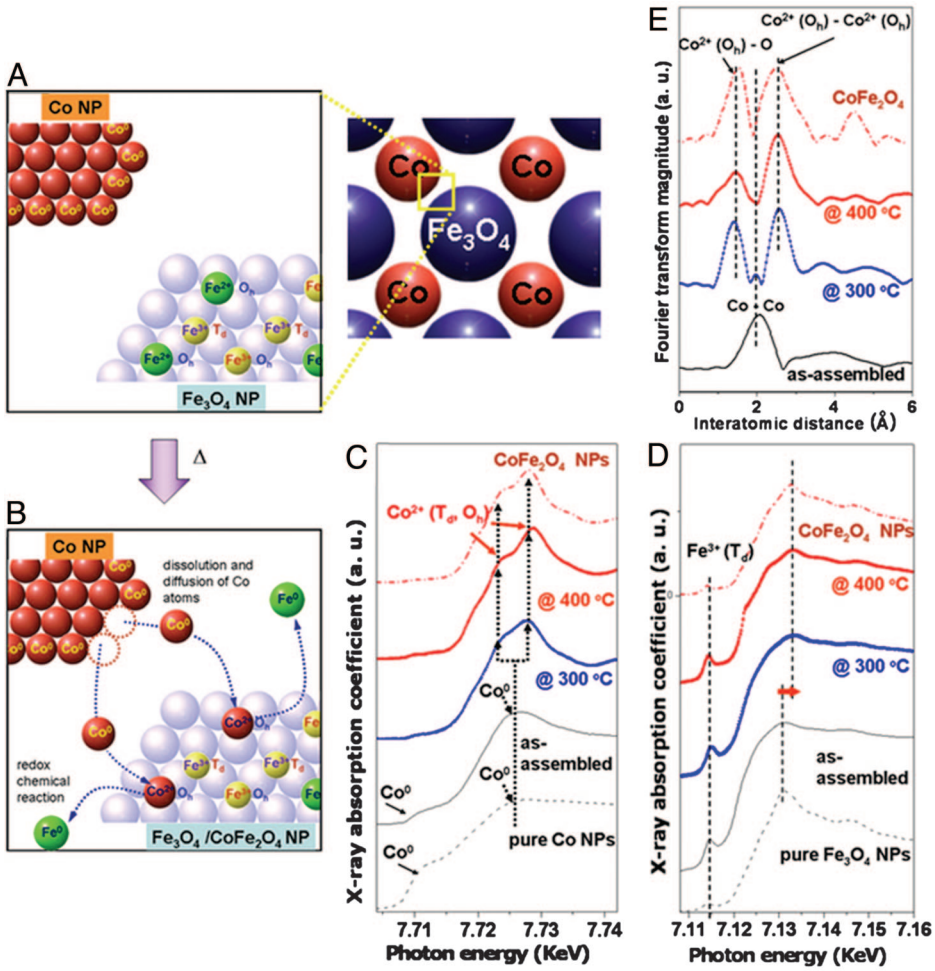

Fig. 5. Nanoscale transformation processes of Fe_3O_4 and Co binary superlattices to core–shell Fe_3O_4@$CoFe_2O_4$ nanoparticle superlattices and the x-ray absorption spectroscopy observations of such processes. (*A* and *B*) Schematic illustrations. Dissolution and diffusion of Co atoms from Co nanoparticles into a Fe_3O_4 inverse spinel matrix and redox chemical exchange between incoming Co and Fe^{2+} in an O_h site, results in the formation of Fe_3O_4@$CoFe_2O_4$. (*C* and *D*) Temperature-dependent x-ray absorption near-edge structure spectra of as-assembled AB-type and annealed superlattices. Upon thermal treatment, in the Co K-edge spectra (*C*), the decrease in intensity of a shoulder at 7,712 eV and the shift of main-edge peak to a higher-energy region indicate oxidation of Co metallic species to Co^{2+}. In the Fe K-edge spectra (*D*), the slight shift of the main-edge peak to higher energy indicates an increase of average Fe oxidation states by gradual loss of Fe^{2+} from O_h sites of the spinel structure. (*E*) Co K-edge extended x-ray absorption fine structure data of as-assembled and annealed superlattices. Upon thermal treatment, significant reduction in the Co–Co scattering at 2.0 Å and appearance of new peaks at 1.7 and 2.6 Å are observed, which indicates the disappearance of metallic Co and the formation of oxidized Co ion of $CoFe_2O_4$ species.

sites (20, 21). Upon thermal annealing, the main-edge peak slightly shifts toward higher energy in both samples at 300° and 400°C, suggesting an increase in oxidation state of Fe in O_h sites (21). Because the population of Fe^{2+} in the O_h site decreases as it is replaced by Co upon the formation of cobalt ferrite, it is reasonable to observe increment of average oxidation state of iron atoms in the O_h sites (21).

Extended x-ray absorption fine structure (EXAFS) analyses provide additional information on the local structural changes around Co atoms during the thermal annealing processes. In the Fourier-transformed Co K-edge EXAFS spectra of the AB-type superlattices (Fig. 5*E*), the peak at 2.0 Å, corresponding to fcc Co–Co at 2.0 Å in as-assembled superlattices, significantly decreased in intensity at 300°C and finally disappeared at 400°C. In contrast, the appearance of two new peaks at 1.7 and 2.6 Å is clearly seen, corresponding to $Co(O_h)$–O and $Co(O_h)$–$Co(O_h)$ scattering of $CoFe_2O_4$, respectively.

Our observation of the nanoscale transformation of Co and Fe_3O_4 binary superlattices into core–shell type Fe_3O_4@$CoFe_2O_4$ superlattices explains the huge enhancements in their magnetism. The Co and Fe_3O_4 nanoparticles are a class of soft magnets, but when such soft–soft magnet superlattices are transformed into the core–shell type soft–hard Fe_3O_4@$CoFe_2O_4$ superlattices, it is possible to have a strong magnetic coupling between a hard magnet $CoFe_2O_4$ shell and the soft Fe_3O_4 core generated through an exchange-coupled magnetic system with high magnetic coercivity (8, 18).

In summary, we have demonstrated the fabrication of highly ordered binary magnetic nanoparticle assemblies with controlled packing geometry through size ratio and stoichiometric effects. The binary superlattices show a unique ferrimagnetic phase transformation behavior through nanoscale redox chemical reactions, which leads to a magnetically soft–hard core–shell type nano-alloy system. The assembly-induced phase transformation strategy presented here can potentially be extended not only for high-performance integrated magnetic systems such as high-density information storage devices and magnetic sensors, but also for the fabrication of new types of ordered nanosystems with multifunctionalities and enhanced properties.

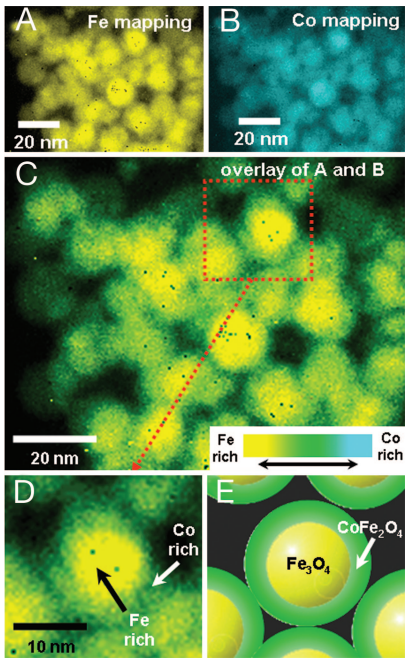

Fig. 6. Elemental mapping analyses of core–shell type Fe_3O_4@$CoFe_2O_4$ nanoparticles using high-resolution TEM. (*A* and *B*) Elemental maps of the core–shell nanoparticles based on Fe L-edge (*A*) and Co-L-edge (*B*) electron energy loss spectroscopy. Iron and cobalt signals are color-coded as yellow and cyan, respectively. (*C–E*) An overlay of Fe and Co maps. Strong yellow color in the core region of a nanoparticle is observed. Green color, which is resulting from color mixing of yellow and cyan, is observed at the shell region of a nanoparticle. These observations support that the core consists of iron-rich materials (i.e., Fe_3O_4) and the shell is comprised of materials containing iron and cobalt (i.e., $CoFe_2O_4$).

Methods

Synthesis of Co Nanoparticles and Fe_3O_4 Nanoparticles. For the synthesis of monodispersed Co nanoparticles (7.5 nm), 4 ml of 0.5 M $Co_2(CO)_8$ was injected into refluxing toluene containing 0.080 g of NaAOT and allowed to react for 6 h. After precipitation by addition of ethanol, Co nanocrystals were redissolved in 40 ml of toluene.

Fe_3O_4 nanoparticles of 8.0, 15.7, and 18.0 nm were synthesized by the thermal decomposition of iron pentacarbonyl [$Fe(CO)_5$; 1 mmol] in a hot octyl ether solution containing 3 mmol of lauric acid under aerobic condition (15). After injection of the precursor solution into hot surfactant solution at 293°C, large nanoparticles were allowed to grow for an appropriate time (1 h for 8.0 nm, 1.5 h for 15.7 nm, and 2 h for 18.0 nm) and then cooled to room temperature. Ethanol was added to precipitate nanoparticles from the solution. The particles were separated by centrifugation and redispersed in toluene.

Binary Structures of Co Nanoparticles and Fe_3O_4 Nanoparticles. Separately prepared Fe_3O_4 and Co nanoparticles were dissolved in toluene (2 mg/ml). Nanoparticle solutions with molar ratios of 1:1 for AB and 1:2 for AB_2 were mixed together, which was followed by slow evaporation (≈10 min) on a carbon-coated Cu grid attached on a glass slide in a Petri dish under an inert Ar atmosphere of 1 atm at room temperature. TEM analysis were performed on EM 912Ω (Zeiss, Korea Basic Science Institute) operated 120 kV whose point resolution is 3.7 Å and ARM 1300S (JEOL, Korea Basic Science Institute) operated at 1,250 kV with a point resolution of 1.2 Å.

Formation of Fe_3O_4@$CoFe_2O_4$ from AB Superlattices. AB superlattices are formed on a TEM grid or a Si wafer (1 cm^2) by slow evaporation of the mixed solution of Fe_3O_4 and Co nanoparticles (≈2 ml) under Ar atmosphere. Thermal transformation processes were conducted on a hot plate preheated to a constant temperature of 300° or 400°C under Ar gas for 1 h. The annealed sample was sealed with polyimide tape (KAPTON-500H, 125-μm thickness) in a glove box to prevent any contamination and analyzed by superconducting quantum interference device, electron energy loss spectroscopy (EELS), and x-ray absorption spectroscopy. EELS mapping analyses were performed through standard three-windows methods with the energy window of 30 eV. Co K-edge, Fe K-edge x-ray absorption spectra were obtained in reflection mode at beamline 7C of Pohang Light Source with a ring current of 120 ~ 170 mA at 2.5 GeV.

We thank J. M. Oh and H. C. Kim (Korea Basic Science Institute). This work is supported in part by Nano Science and Technology Grant M1-0213-12-0001, National Core Research Center Grant R15-2004-024-02002-0, R & D Program of Fusion Strategies for Advanced Technologies Grant M1-0326-11-0006, NCI Center for Nanotechnology Excellence, Center for Nanotubes and Nanostructured Composites, and the BK 21 Project.

1. Sun, S., Murray, C. B., Weller, D., Folks, L. & Moser, A. (2000) *Science* **287,** 1989–1992.
2. Markovich, G., Collier, C. P., Henrichs, S. E., Remacle, F., Levine, R. D. & Heath, J. R. (1999) *Acc. Chem. Res.* **32,** 415–423.
3. Murray, C. B., Kagan, C. R. & Bawendi, M. G. (1995) *Science* **270,** 1335–1338.
4. Whetten, R., Shafigullin, M. N., Khoury, J. T., Schaaff, T. G., Vezmar, I., Alvarez, M. M. & Wilkinson, A. (1999) *Acc. Chem. Res.* **32,** 397–406.
5. Sanders, A. E. & Korgel, B. A. (2005) *ChemPhysChem* **6,** 61–65.
6. Kiely, C. J., Fink, J., Brust, M., Bethell, D. & Schiffrin, D. J. (1998) *Nature* **396,** 444–446.
7. Kiely, C. J., Fink, J., Zheng, J. G., Brust, M., Bethell, D. & Schiffrin D. J. (2000) *Adv. Mater.* **12,** 640–643.
8. Redl, F. X., Cho, K.-S., Murray, C. B. & O'Brien, S. (2003) *Nature* **423,** 968–971.
9. Zeng, H., Li, J., Liu, J. P., Wang, Z. L. & Sun, S. (2002) *Nature* **420,** 395–398.
10. Shevchenko, E. V., Talapin, D. V., Kotov, N. A., O'Brien, S. & Murray, C. B. (2006) *Nature* **439,** 55–59.
11. Trizac, E., Eldridge, M. D. & Madden, P. A. (1997) *Mol. Phys.* **90,** 675–678.
12. Sanders, J. V. & Murray, M. J. (1980) *Philos. Mag. A* **42,** 705–720.
13. Murray, M. J. & Sanders, J. V. (1980) *Philos. Mag. A* **42,** 721–740.
14. Shevchenko, E. V., Talapin, D. V., O'Brien, S. & Murray, C. B. (2005) *J. Am. Chem. Soc.* **127,** 8741–8747.
15. Cheon, J. Kang, N.-J., Lee, S.-M., Lee, J.-H., Yoon, J.-H. & Oh, S. J. (2004) *J. Am. Chem. Soc.* **126,** 1950–1951.
16. Park, J.-I., Kang, N.-J., Jun, Y.-w., Oh, S. J., Ri, H.-C. & Cheon, J. (2002) *ChemPhysChem* **3,** 543–547.
17. McCurrie, R. A. (1994) *Ferromagnetic Materials: Structure and Properties* (Academic, London).
18. Kishimoto, M. (1979) *J. Appl. Phys.* **50,** 450–452.
19. Cheng, G., Carter, J. D. & Guo, T. (2004) *Chem. Phys. Lett.* **400,** 122–127.
20. Ammar, S. Helfen, A., Jouini, N., Fiévet, F., Rosenman, I., Villain, F., Molinié, P. & Danot M. (2001) *J. Mater. Chem.* **11,** 186–192.
21. Matsumoto, K., Saito, F., Toyoda, T., Ohkubo, K., Yamawaki, K., Moril, T., Hiranol, K., Tanakal, M. & Sasaki, S. (2000) *Jpn. J. Appl. Phys.* **39,** 6089–6093.